RSC Advances

PAPER

View Article Online
View Journal | View Issue

Open Access Article. Published on 22 May 2017. Downloaded on 12/6/2025 2:02:47 AM.
This article is licensed under a Creative Commons Attribution 3.0 Unported Licence.

Check for updates

Cite this: *RSC Adv.*, 2017, 7, 26943

Carbon quantum dot sensitized Pt@Bi_2WO_6/FTO electrodes for enhanced photoelectro-catalytic activity of methanol oxidation

Huajun Zheng, *[ab] Ping Niu[a] and Zhefei Zhao[a]

Carbon quantum dot sensitized Pt@Bi_2WO_6/FTO electrodes (simplified as CQDs-Pt@Bi_2WO_6/FTO) were successfully prepared by loading platinum particles onto Bi_2WO_6 nanoplates *via* a photo-deposition method and sensitized carbon quantum dots (CQDs) *via* a dip-coating method. The photoelectro-catalytic properties of the Pt@Bi_2WO_6/FTO and CQDs-Pt@Bi_2WO_6/FTO electrodes for methanol oxidation were investigated. The results indicated that the CQDs-Pt@Bi_2WO_6/FTO electrode shows higher photoelectro-catalytic activity and better stability than that of the Pt@Bi_2WO_6/FTO electrode. The higher photoelectro-catalytic performance for methanol oxidation was attributed due to the special synergetic effects between the photocatalytic and electrocatalytic process under solar light irradiation. More importantly, the introduction of CQDs broaden the photoresponse range of the Bi_2WO_6 material and improves the mobility of the photocarriers. Meanwhile, the doped CQDs act as preferential adsorption sites for the intermediate carbonaceous species during methanol oxidation. This not only alleviates CO poisoning towards the Pt particles, but also improves the efficiency of methanol oxidation by constructing a new type of CQDs-Pt electrocatalyst. The composite material, which combines the dual function of photocatalysis and electrocatalysis will be a promising candidate for new photoelectro-catalytic fuel cells.

Received 14th February 2017
Accepted 4th May 2017

DOI: 10.1039/c7ra01867c

rsc.li/rsc-advances

1. Introduction

Direct methanol fuel cells (DMFCs), as an environmentally friendly energy conversion technology, have attracted more and more attention in recent decades.[1–5] The key factor of the industrial application of DMFCs is a catalyst with high electrocatalytic activity and a long-duration of stability.[6] To date, platinum-based electrodes, as one of the best catalytic materials, have been widely used in the electrocatalytic oxidation of methanol. However, the major limitations of platinum-based materials are that they are expensive and easily poisoned *via* strong CO adsorption on its active sites.[7] One effective strategy to reduce the amount of precious metals in the catalysts and improve their performance is the development of an innovative type of photoelectrocatalyst, which loads less precious metal (such as Pt, Au, Ru and Ag) particles onto photocatalysts. The photocatalytic oxidation of methanol takes place on the photocatalyst under solar light illumination and the oxidation reaction will be simultaneously electrocatalysed by the precious metal particles. Recently, more photoelectrocatalysts have been developed as anode materials used for methanol oxidation.[8–11] Pt nanoparticles doped on TiO_2 nanotubes (Pt-NPs/TNTs) were fabricated for alternative anode materials. The Pt-NPs/TNTs electrodes significantly enhanced the electrocatalytic performance and stability for methanol oxidation. The oxidation peak currents on the Pt-NPs/TNTs electrodes are several times larger than those on a platinum electrode and the photocatalytic properties of the TiO_2 make the Pt-NPs/TNTs electrode reusable after a short UV treatment.[12] From the point of view of their nature, the anode materials for methanol oxidation reaction should use a photocatalyst with a strong oxidation ability as a substrate. As known, bismuth tungstate (Bi_2WO_6) is one of the simplest members of the Aurivillius compounds with a special layered structure, which can respond to visible-light up to 460 nm.[13] The more attractive merits of Bi_2WO_6 are its strong oxidation ability with the lower valence band potential (3.2 eV *vs.* NHE). In fact, Bi_2WO_6 materials comprised of various complicated 3D hierarchical nanostructures have been synthesized and used as the substrate for noble metals. Zhang *et al.* have reported that Ag nanoparticles can be firmly anchored on a Bi_2WO_6 heterostructure *via* a photo-deposition method. The decoration of Ag effectively broadened the visible-light response of Bi_2WO_6 and inhibited the recombination of the photogenerated electron–hole pairs. The synergistic effect between Ag and Bi_2WO_6 resulted in an optimum photodegradation efficiency with a rate constant 3.1-folds greater than Bi_2WO_6.[13]

[a]*Department of Applied Chemistry, Zhejiang University of Technology, Hangzhou 310032, China. E-mail: zhenghj@zjut.edu.cn*

[b]*State Key Laboratory Breeding Base of Green Chemistry Synthesis Technology, Zhejiang University of Technology, Hangzhou 310032, China*

Open Access Article. Published on 22 May 2017. Downloaded on 12/6/2025 2:02:47 AM. This article is licensed under a Creative Commons Attribution 3.0 Unported Licence.

Methanol is oxidized to various intermediate carbonaceous species (such as CO, –CHO, –COOH and CH_4) according to various oxidation process and reaction pathways.[14] The intermediate carbonaceous species (mainly CO) are easily adsorbed on the electrode surface, blocking the active sites and significantly slows the overall reaction. Therefore, an important method to improve the catalytic stability is to alleviate CO poisoning towards the platinum-based electrocatalyst. One solution is to reduce the intermediate production by controlling the oxidation process. When more holes or $OH^{\bullet}$ with high activity gather around the active sites on the surface of the anode in the electrocatalytic oxidation of methanol, the $OH^{\bullet}$ facilitates the local methanol concentration to the neighbor noble metal[1,9] and then can oxidize intermediate CO,[2] including the methanol molecules. Another solution is the construction of a Pt–M bimetallic catalyst with a second metal M (M = Ru, Co, Ni, Fe, Mn), which allows the oxidation of CO at a lower potential than with Pt. Pt–Ru alloys in particular have been shown to be especially successful in the prevention of Pt catalyst poisoning.[15]

Recently, carbon quantum dots (CQDs) have been introduced to semiconductor materials, including CQDs/TiO_2,[16] CQDs/WO_3,[17,18] CQDs/Fe_3O_4,[19] CQDs/BiOX,[20–22] CQDs/Bi_2WO_6,[23] CQDs/Bi_2MoO_6 (ref. 24) and CQDs/$BiVO_4$,[25] due to their excellent electron transfer ability. Chang *et al.* have fabricated $Cu_{2-x}S$/carbon nanodots (C dots) electrodes for direct methanol fuel cells and the EIS results revealed that it has a lower charge-transfer resistance.[26] Moreover, CQDs can act as the preferential adsorption sites for carbon monoxide to achieve the transfer of the CO adsorption sites, reducing the adsorption of CO on Pt. Then, the CO adsorbed on CQDs will be oxidized by $OH^{\bullet}$,[2] which is produced *via* Bi_2WO_6 photocatalysis. Therefore, the CQDs-Pt catalyst will be beneficial in reducing the incidence of CO poisoning towards the Pt particles and improve the efficiency of methanol oxidation.

In this paper, we demonstrate our strategy for designing a novel bifunctional catalyst (CQDs-Pt@Bi_2WO_6/FTO), which is based on Bi_2WO_6 nanoplates as a photocatalyst and platinum particles as an electrocatalyst. By doping CQDs into the Pt@Bi_2WO_6 nanoplates, not only do they increase the photocatalytic activity of Bi_2WO_6 and improve the utilization of solar energy, but also the sensitized CQDs are the preferential absorption sites for the intermediate carbonaceous species, which can alleviate CO poisoning towards the Pt particles. Therefore, the CQDs-Pt@Bi_2WO_6/FTO electrode reveals excellent catalytic activity and better stability, and is a potential candidate for photoelectro-catalytic cells.

2. Experimental

2.1 Materials and reagents

Ethanol, nitric acid, hydrochloric acid, citric acid, sodium hydroxide, chloroplatinic acid (H_2PtCl_6), sodium tungstate ($Na_2WO_4 \cdot 2H_2O$) and bismuth nitrate ($Bi(NO_3)_3 \cdot 5H_2O$) were purchased from Aladdin. All the reagents were of analytical grade and were used without any further purification. Fluorine-doped tin oxide (FTO) conducting glass (15 × 50 mm) was purchased from Yinkou Opvtech Co., Ltd. Deionized Water was obtained from a Hitech-K flow water purification system.

2.2 Preparation of the Bi_2WO_6/FTO sample

The Bi_2WO_6/FTO samples were prepared *via* a hydrothermal reaction from unfired WO_3/FTO samples. The WO_3/FTO samples were prefabricated according to a method, which has been reported in our previous work.[18,27] In a typical run, 4 mmol of $Bi(NO_3)_3 \cdot 5H_2O$ was dissolved into 50 mL of 5% dilute nitric acid and was stirred until the solution became transparent. Then, the transparent liquid was added into an 80 mL Teflon-lined autoclave and the WO_3/FTO was vertically placed into it. The autoclave was sealed in a stainless steel tank and heated at 160 °C for 24 h. Subsequently, the reactor was allowed to cool down to room temperature naturally. The resulting samples were taken out and washed with deionized water and absolute ethyl alcohol, and then dried in air for 0.5 h. Subsequently, thermal treatment of the Bi_2WO_6/FTO was carried out at 400 °C in air for 4 h at a ramping rate of 2 °C min^{-1}.

2.3 Preparation of the CQDs-Pt@Bi_2WO_6/FTO sample

The Pt@Bi_2WO_6/FTO sample was prepared *via* a photo-deposition method. The as-prepared Bi_2WO_6/FTO sample was immersed in 0.5 mM H_2PtCl_6 and was irradiated with UV and visible light for 1 h. Subsequently, the Pt@Bi_2WO_6/FTO sample was completed after washing with deionized water and ethanol. The obtained films were dried overnight at 60 °C.

The CQDs-Pt@Bi_2WO_6/FTO samples were prepared *via* a dip-coating method. The CQDs were synthetized according to a literature procedure followed by a thermal treatment.[28] The as-prepared Pt@Bi_2WO_6/FTO sample was immersed in a specified concentration of CQDs aqueous solution for 1 h. Finally, the CQDs-Pt@Bi_2WO_6/FTO samples were obtained by washing with deionized water and dried in air.

2.4 Photocatalyst characterization

The morphology, microstructure and chemical composition of the samples were observed using transmission electron microscopy (TEM, JEOL, JEM-2010) and scanning electron microscopy (SEM, Hitachi S+4800) with the elemental mapping images and EDX. Powder X-ray diffraction (XRD, Bruker D8 with Cu-Kα radiation) experiments were carried out to analyze the crystallographic structural information of the samples. X-ray photoelectron spectroscopy (XPS, Thermo Fisher Scientific, USA) was performed using an ESCALab MKII spectrometer with Al Kα (1.4866 keV) as the X-ray source. The UV-vis diffuse reflectance spectra of the samples were recorded on a UV2700 type spectrophotometer.

2.5 Photocatalytic(PC) and photoelectron-catalytic(PEC) measurement

The photocurrent responses were investigated using a three-electrode system using an electrochemical workstation (CHI 760D), wherein the modified Bi_2WO_6/FTO electrode, platinum plate (1 cm × 1 cm) and saturated calomel electrode (SCE)

 This journal is © The Royal Society of Chemistry 2017

Open Access Article. Published on 22 May 2017. Downloaded on 12/6/2025 2:02:47 AM.
This article is licensed under a Creative Commons Attribution 3.0 Unported Licence.

served as the working electrode, the counter electrode and the reference electrode, respectively. A mixed solution of 1.0 M KOH and 0.5 M CH_3OH was used as the electrolyte. Before the experiments, all the solutions were purged with nitrogen for 30 min in order to exclude O_2. Electrochemical impedance spectroscopy (EIS) was recorded between 0.1 and 10^5 Hz with an AC voltage amplitude of 5.0 mV. All PEC measurements were under a solar light simulator with a 150 W Xenon arc lamp (Beijing, Perfect Labsolar 300). The light intensity was measured to be 100 mW cm^{-2}. Amperometric *I–t* curves were obtained at 0 V (*vs.* SCE) with light on-off switches of 20 s.

3. Results and discussion

3.1 Structure and morphology

The surface morphologies of the as-prepared samples were characterized by SEM. Fig. 1 depicts the SEM images of the Bi_2WO_6/FTO and CQDs-Pt@Bi_2WO_6/FTO samples. The growth mechanism of the WO_3 nanoplates on surface of the FTO glass has been reported in our previous study.[19,28] In this work, WO_3 can be converted to Bi_2WO_6 because the unfired WO_3 film contains water molecules and the $(Bi_2O_2)^{2+}$ units can replace the water molecules during the hydrothermal process.[29] Fig. 1a shows the SEM images of the uniform Bi_2WO_6 nanoplates with a thickness of 20–30 nm. From the cross-sectional SEM image of the Bi_2WO_6/FTO sample, as shown in Fig. 1b, it can be clearly seen that the Bi_2WO_6 layer with the thickness around 2–2.5 μm was vertically grow on the FTO glass. When the photo-deposition reaction and dip-coating steps were carried out in turn, the platinum particles were successfully deposited on the surface of the Bi_2WO_6/FTO nanoplates, which can be observed in the magnified SEM images. As shown in Fig. 1c and d, the morphology of the Bi_2WO_6/FTO nanoplates did not change, however, the surface becomes rough. Direct evidence of the deposited Pt comes from the element mapping spectrum (elements distribution of Pt, Bi, W, O and C) of the CQDs-Pt@Bi_2WO_6/FTO sample (Fig. 1e). It was found that the Pt elements were evenly distributed on the surface of the nanoplates, which confirms that the Pt particles were photo-deposited on the surface of the nanoplates. This is also supported by the energy dispersive X-ray spectroscopy (EDX) results and the content of the Pt, Bi, W, O and C elements were measured in Fig. 1f, respectively.

More interestingly, the C element from the mapping spectrum and its contents from the EDX spectrum provided some information on the CQDs adsorbed on the Pt@Bi_2WO_6/FTO sample. It is difficult to observe any change in the morphology of the original substance because a small quantity of CQDs is loaded *via* simple electrostatic adsorption. However, evidence of their existence on the surface of the Bi_2WO_6 nanoplates can be further provided by the high-resolution transmission electron microscopy (HRTEM) images. The HRTEM image in Fig. 2 shows the uniform decoration of the CQDs throughout the surface of the Bi_2WO_6 nanoplates and the lattice spacing of the CQDs (Fig. 2b) is about 0.321 nm, which can be ascribed to the (002) crystallographic planes of the CQDs. These results are consistent with the observations previously reported.[30]

The surface compositions and chemical states of CQDs-Pt@Bi_2WO_6/FTO were analysed by XPS and the results are displayed in Fig. 3. The typical survey scans in Fig. 3a display the five elements of Bi, W, O, C and Pt. The trace amount of C was more likely to come from the carbon quantum dots. Fig. 3b–f shows the high resolution XPS spectra of Bi 4f, W 4f, O 1s, C 1s and Pt 4f, respectively. The peaks in Fig. 3b at 164.4 and 159.1 eV correspond to the Bi $4f_{5/2}$ and Bi $4f_{7/2}$ orbitals of Bi^{3+}. The peaks at 37.2 and 35.0 eV correspond to the W $4f_{5/2}$ and W $4f_{7/2}$ orbitals of W^{6+}, as shown in Fig. 3c. The convoluted peaks at 530.2 and 532.6 eV of O 1s in Fig. 3d were consistent with the different chemical environments of the oxygen element in Bi–O

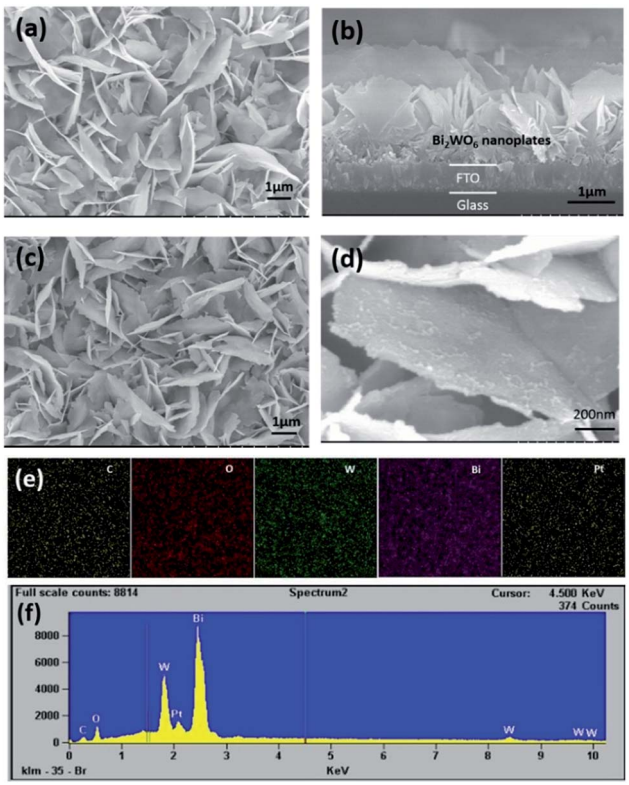

Fig. 1 SEM images of the as-prepared samples: Bi_2WO_6/FTO (a), (b) and CQDs-Pt@Bi_2WO_6/FTO (c), (d). The elemental mapping image (e) and EDX spectrum (f) for CQDs-Pt@Bi_2WO_6/FTO.

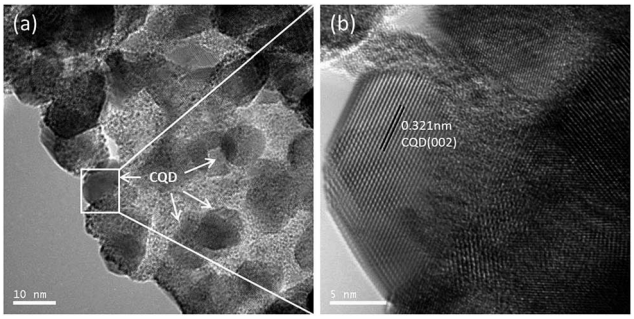

Fig. 2 (a) TEM and (b) HRTEM images of the as-prepared sample: CQDs@Bi_2WO_6/FTO.

Open Access Article. Published on 22 May 2017. Downloaded on 12/6/2025 2:02:47 AM.
This article is licensed under a Creative Commons Attribution 3.0 Unported Licence.

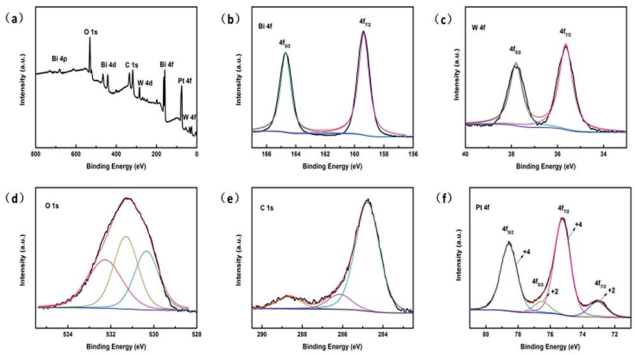

Fig. 3 The XPS spectra of the CQDs-Pt@Bi_2WO_6/FTO: (a) Full scan, (b) Bi 4f, (c) W 4f, (d) O 1s, (e) C 1s and (f) Pt 4f.

and W–O.[31] The peak at 531.4 eV corresponds to the hydroxyl groups on the surface of Bi_2WO_6. Fig. 3e shows the C 1s spectra of CQDs-Pt@Bi_2WO_6/FTO. By using a Gaussian fitting, the C 1s spectra can be deconvoluted into three peaks (284.6, 286.26 and 288.38 eV), which were ascribed to the C–C, C–O and C=O bonds, respectively.[23] The high-resolution Pt 4f spectrum can be deconvoluted into four peaks as shown in Fig. 3f. The strong signals, two peaks at a low binding energy of 74.85 eV and a high binding energy at 78.5 eV, are because of the Pt^{4+} species, suggesting that Pt in the CQDs-Pt@Bi_2WO_6/FTO was mainly in the form of $Pt(OH)_4$. The relatively weak peaks located at 73.1 and 76.5 eV can be signed to the Pt^{2+} chemical state.[32,33]

Fig. 4 displays the XRD patterns of the Bi_2WO_6/FTO, CQDs-Bi_2WO_6/FTO and CQDs-Pt@Bi_2WO_6/FTO samples. For Bi_2WO_6/FTO sample, the peaks at 28.3°, 32.9°, 47.2°, 55.8°, 76.0° and 78.5° correspond to the (131), (002), (202), (331), (210) and (204) planes of orthorhombic Bi_2WO_6 (JCPDS: 39-0256). The peaks at 26.6°, 33.8°, 51.8°, 61.7°, 65.7° correspond to the (110), (101), (211), (310) and (301) planes of FTO (JCPDS: 46-1088). No peaks indicating impurities are observed, demonstrating that the WO_3 have been completely translated into Bi_2WO_6 and the final samples have good crystallinity and purity. After the deposition of the Pt nanoparticles and CQDs doping, the main peaks of both the CQDs@Bi_2WO_6/FTO and CQDs-Pt@Bi_2WO_6/FTO samples were almost identical to Bi_2WO_6/FTO, which suggests the composites do not change the crystal structure of Bi_2WO_6. The results also indicate that the CQDs and Pt contents in CQDs-Pt@Bi_2WO_6/FTO samples were very rare.

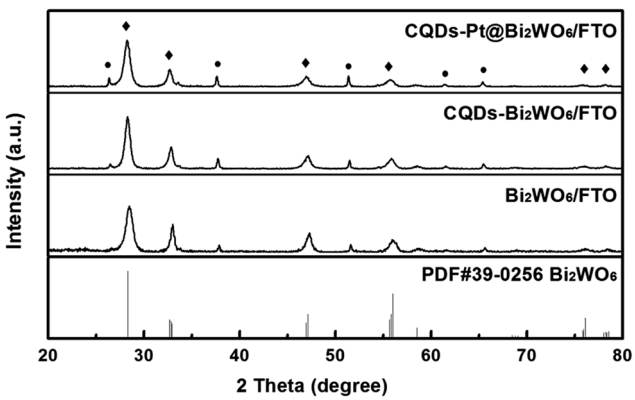

Fig. 4 The XRD patterns of Bi_2WO_6/FTO, CQDs-Bi_2WO_6/FTO and CQDs-Pt@Bi_2WO_6/FTO.

3.2 Optical absorption properties

The optical absorption properties of the Bi_2WO_6/FTO, CQDs-Bi_2WO_6/FTO, Pt@Bi_2WO_6/FTO and CQDs-Pt@Bi_2WO_6/FTO samples were investigated using UV-vis spectrophotometry and the results are shown in Fig. 5a. The UV-vis diffuse reflectance spectrum of the Bi_2WO_6/FTO sample showed the absorption edge at ~450 nm. When it was sensitized by the CQDs, a small red-shift was observed in the absorption edge and the absorption edge of the CQDs@Bi_2WO_6/FTO sample increases to 470 nm. Similar results were observed in the Pt@Bi_2WO_6/FTO sample after doped CQDs. The photo-response range of the Pt@Bi_2WO_6/FTO sample was around 500 nm and the range of the CQDs-Pt@Bi_2WO_6/FTO sample was up to 510 nm. Similarly, because the presence of the metallic Pt particles contributes to the enhanced absorption in the visible light region, the range of light absorption for the Pt@Bi_2WO_6/FTO sample was wider than

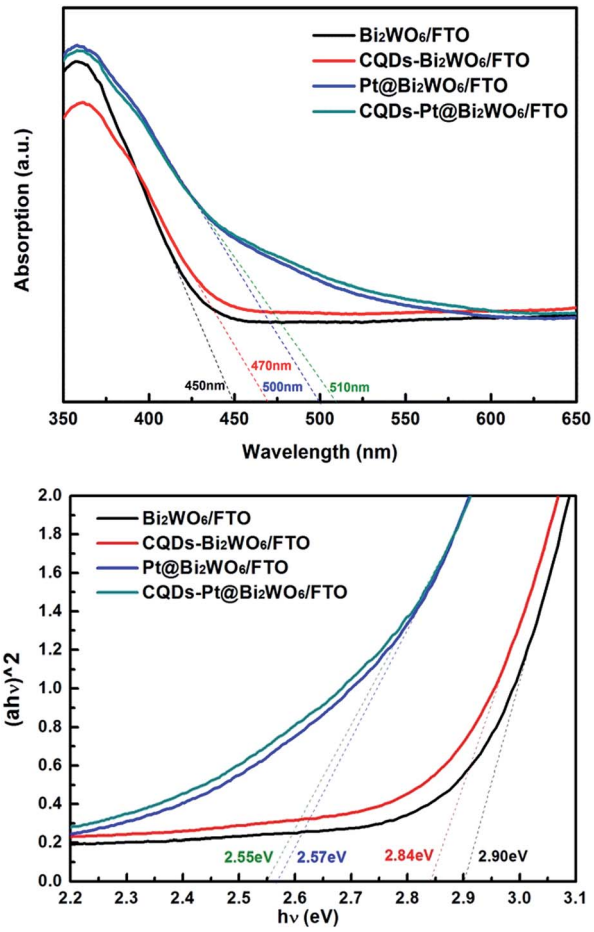

Fig. 5 The UV-vis diffuse reflectance spectra (a) and Tauc plots of the corresponding absorption spectra (b) of Bi_2WO_6/FTO, CQDs-Bi_2WO_6/FTO, Pt@Bi_2WO_6/FTO and CQDs-Pt@Bi_2WO_6/FTO.

Open Access Article. Published on 22 May 2017. Downloaded on 12/6/2025 2:02:47 AM.
This article is licensed under a Creative Commons Attribution 3.0 Unported Licence.

that of the Bi_2WO_6/FTO sample. This phenomenon is highly consistent with the previous reports.[34]

The band gap energies of the four type samples were calculated based on the Tauc plot:

$$\alpha h\nu = A\,(h\nu - E_g)^n$$

where h is the Planck's constant, ν is the frequency of the vibration, α is the absorption coefficient, E_g is the band gap of the semiconductor and n is a constant, which is 1/2 for a direct transition or 2 for an indirect transition.[35] For the Bi_2WO_6 semiconductor, n is equal to 1/2. The calculated E_g values of Bi_2WO_6/FTO, CQDs-Bi_2WO_6/FTO, Pt@Bi_2WO_6/FTO and CQDs-Pt@Bi_2WO_6/FTO sample were 2.90, 2.84, 2.57 and 2.55 eV, respectively (Fig. 5b). Obviously, the band gap of the sample is decreased after being doped with the CQDs and the photo-deposition of the Pt particles.

3.3 Methanol oxidation

The photocatalytic oxidation abilities towards methanol on the Bi_2WO_6/FTO and CQDs-Bi_2WO_6/FTO electrodes were investigated using the amperometric I–t curves (photocurrent response) under light illumination conditions in 1 M KOH or 1 M KOH + 0.5 M CH_3OH aqueous solution. There are two main factors that may affect the photocurrent density. One is the oxygen evolution reaction (OER) and the other is the methanol oxidation reaction (MOR). The photocurrent density of the electrode in 1 M KOH aqueous solution was attributed to the OER, while that in 1 M KOH + 0.5 M CH_3OH aqueous solution was attributed to both the OER and MOR. As shown in Fig. 6, the photocurrent density on both the Bi_2WO_6/FTO and CQDs-Bi_2WO_6/FTO electrodes can be measured in two types of electrolytes. This phenomenon can be explained by the valence band potential of Bi_2WO_6 being relatively positive, which indicates that Bi_2WO_6 has a stronger photocatalytic oxidation ability for the OER and MOR. More importantly, there was a significant increase in the photocurrent density of the Bi_2WO_6/FTO electrode upon CQDs doping (Fig. 6b), whether in the presence of methanol or not. This may be due to the strong ability of the CQDs to capture and transfer the photo-generated carriers.[36] Furthermore, both the Bi_2WO_6/FTO and CQDs-Bi_2WO_6/FTO electrodes in the absence of methanol are severely reduced with an increase in time. On the contrary, the photocurrent densities of both electrodes in 1 M KOH + 0.5 M CH_3OH aqueous solution show an increasing tendency and then reach a plateau. The total photocurrent density of the Bi_2WO_6/FTO and CQDs-Bi_2WO_6/FTO electrode reached 0.044 and 0.068 mA cm^{-2}, and the other from the MOR are 0.032 and 0.048 mA cm^{-2}, respectively. This confirmed the excellent photocatalytic properties for methanol oxidation on the Bi_2WO_6/FTO and CQDs-Bi_2WO_6/FTO electrodes.

Cycle voltammetry (CV) was employed to examine the electrocatalytic and photoelectro-catalytic performance of the Pt@Bi_2WO_6/FTO and CQDs-Pt@Bi_2WO_6/FTO electrodes for methanol oxidation. The CV curves obtained for these electrodes at the 100th cycle are shown in Fig. 7a and b, which were carried out in an 1 M KOH + 0.5 M CH_3OH aqueous solution at

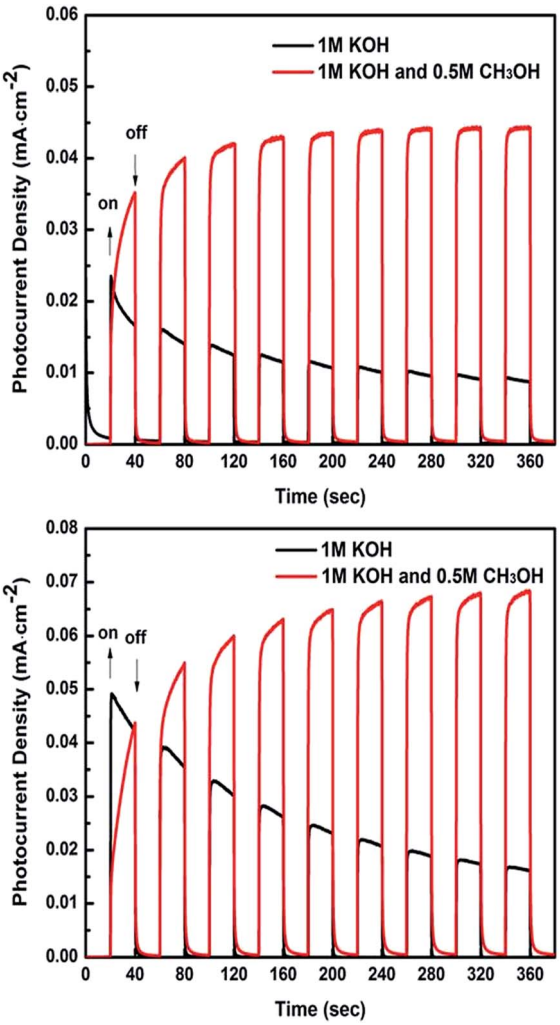

Fig. 6 The I–t curves of the (a) Bi_2WO_6/FTO and (b) CQDs-Bi_2WO_6/FTO samples; the measurements were conducted at 0 V (*vs.* SCE) under a 150 W Xenon arc lamp.

a scan rate of 50 mV s^{-1} with or without solar light, respectively. Undoubtedly, the reaction on the electrodes without solar light illumination is an electrochemical process, while both the electrocatalytic and photocatalytic methanol oxidation processes are under light irradiation. From Fig. 7a and b, whether under solar light illumination or not, it is obvious that the classical phenomena of electrocatalytic methanol oxidation can be observed, that is, a double oxidation peak both in the forward sweep and backward sweep. The forward peak current density (I_f) and the backward peak current density (I_b) of the two type of electrodes with and without solar light illumination are listed in Table 1. Obviously, the Pt particles attached on the Bi_2WO_6/FTO electrode play the main role in the electrochemical methanol oxidation and the effect of Bi_2WO_6/FTO for methanol oxidation should be in the photocatalytic oxidation and synergistic effect for electro-oxidation.

In order to study the role of Bi_2WO_6, Pt/FTO was firstly investigated using CV. For the Pt/FTO electrode, the forward peak current density and the backward peak current density

Open Access Article. Published on 22 May 2017. Downloaded on 12/6/2025 2:02:47 AM.
This article is licensed under a Creative Commons Attribution 3.0 Unported Licence.

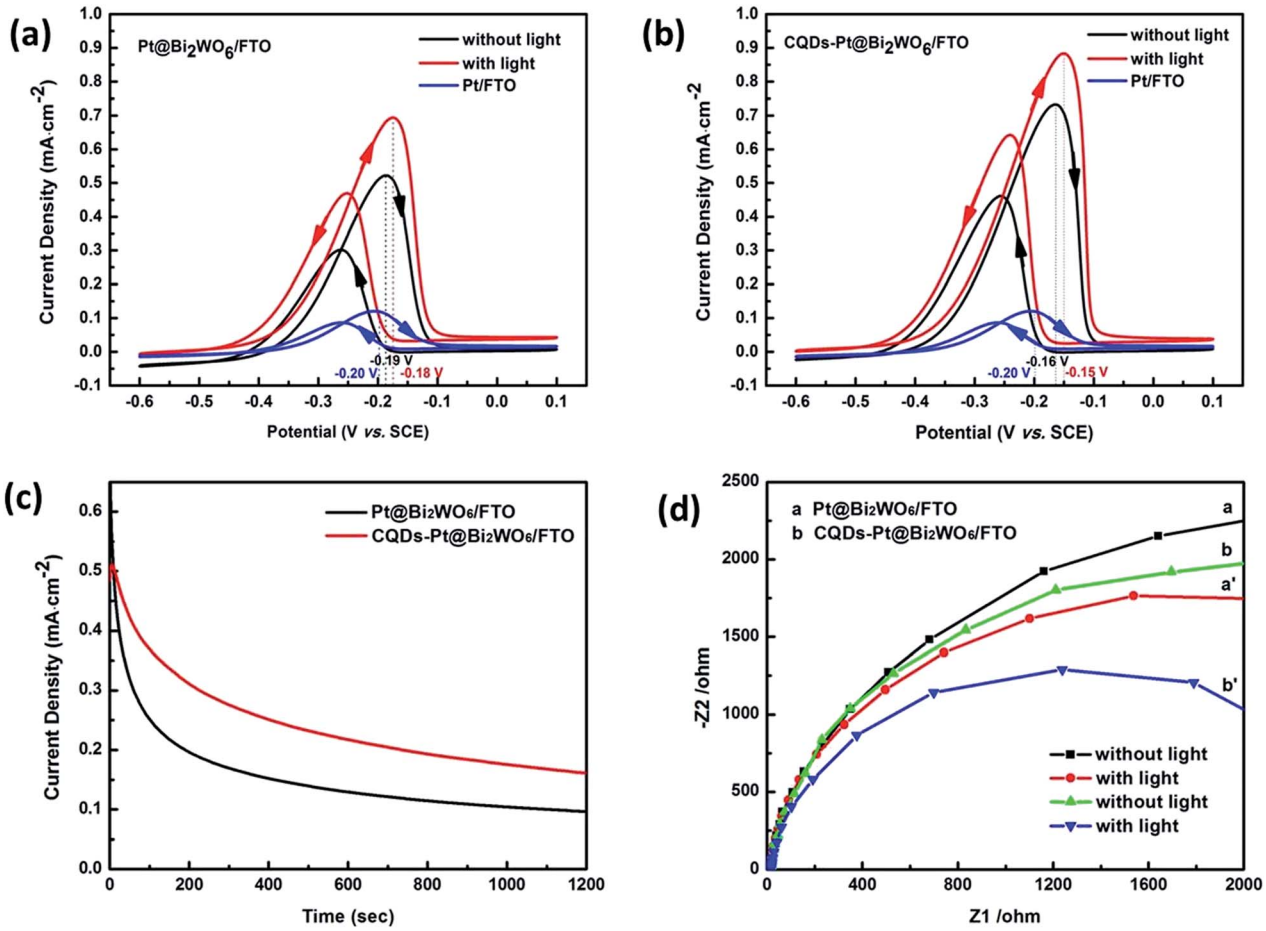

Fig. 7 The 100th cycle voltammetry curves of the (a) Pt@Bi_2WO_6/FTO and (b) CQDs-Pt@Bi_2WO_6/FTO electrodes compared to the Pt/FTO electrode without light in 1.0 M KOH + 0.5 M CH_3OH at a scan rate of 50 mV s^{-1}. (c) The chronoamperometry curves of the electrodes under solar light in 1.0 M KOH + 0.5 M CH_3OH at a potential of −0.2 V (*vs.* SCE) for 1200 s. The EIS of the (d) Pt@Bi_2WO_6/FTO and (b) CQDs-Pt@Bi_2WO_6/FTO electrodes with or without solar light illumination.

Table 1 The electrocatalytic and photoelectro-catalytic parameters of the different electrodes

	Pt@Bi_2WO_6/FTO		CQDs-Pt@Bi_2WO_6/FTO	
Electrode	Electro-oxidation	Photoelectro-oxidation	Electro-oxidation	Photoelectro-oxidation
I_f (mA cm^{-2})	0.52	0.70	0.73	0.89
I_b (mA cm^{-2})	0.30	0.48	0.45	0.64

without light reaches 0.12 and 0.09 mA cm^{-2}, respectively. In addition, the methanol oxidation peak appears accordingly at the potentials of −0.20 and −0.27 V (*vs.* SCE), respectively. For the Pt@Bi_2WO_6/FTO electrode, as shown in Fig. 7a, it can be perceived that the forward peak current density (0.52 mA cm^{-2}) and the backward peak current density (0.30 mA cm^{-2}) without light are ∼4.3 and 3.33 times higher than that from the Pt/FTO electrode, respectively. In addition, the methanol oxidation double peaks appear accordingly at the potentials of −0.19 and −0.26 V (*vs.* SCE), respectively, which is consistent with the literature.[37] When compared with Pt/FTO, the potential is positive (0.01 V). The enhanced peak current density and the positive potential were due to the fact that Bi_2WO_6 acts as a cooperative catalyst and a Pt support material to improve the electrocatalytic performance.[8] Under solar light irradiation, the forward and backward peak current density for methanol oxidation remarkably increases to 0.70 and 0.48 mA cm^{-2}, and the peak potentials also positive shift to −0.18 and −0.25 V. The positive shift in the potential after illumination is also consistent with the literature.[10] The increased peak current density (0.18 mA cm^{-2}) and the positive shifted peak potential (0.01 V) can be attributed to photocatalytic oxidation from the Bi_2WO_6 nanoplates and their synergistic effect between electro-oxidation and photoelectro-oxidation. For the CQDs-Pt@Bi_2WO_6/FTO electrode, as shown in Fig. 7b, the two oxidation peak current densities without light are 0.73 and 0.45 mA cm^{-2}, and

Open Access Article. Published on 22 May 2017. Downloaded on 12/6/2025 2:02:47 AM.
This article is licensed under a Creative Commons Attribution 3.0 Unported Licence.

their corresponding potentials are −0.16 and −0.25 V, respectively. When compared with Pt/FTO, the forward peak current density and the backward peak current density of the CQDs-Pt@Bi_2WO_6/FTO electrode without light are ∼6.08 and 5.00 times higher and the corresponding potential is positive (0.04 V). Similarly, when receiving solar light irradiation, the photoelectro-oxidation of methanol takes place, which brings about further increased peak current densities and further positively shifted peak potentials. The highest forward and backward peak current density reaches 0.89 and 0.64 mA cm^{-2}, and the peak potentials are positively shifted to −0.15 and −0.24 V, respectively. When compared with the oxidation peak current densities and peak potentials of the two electrodes under solar light irradiation, it clearly reveals that the CQDs provide a promotion effect on the photoelectro-oxidation of methanol. Just as the energy gap of the sample can be decreased by CQDs doping, the take-off and peak potentials were visibly positively shifted. This further infers that the CQDs act as electron acceptors to extract the photogenerated electrons from the Bi_2WO_6 nanoplates and transfer to the Pt particles. What's more, the lower peak potential and higher current density are essentially practical from an economical point of view.

The chronoamperometry curves of the CQDs-Pt@Bi_2WO_6/FTO and Pt@Bi_2WO_6/FTO electrodes were measured in 1 M KOH + 0.5 M CH_3OH at a potential of −0.2 V (*vs.* SCE) for 1200 s to verify the stability of the electrodes.[38] As shown in Fig. 7c, the current density of the two types of electrodes decays quickly during the initial 200 s. De Dios and Salgueirino considered that this is because the as-generated intermediate species (mainly CO) are absorbed on the active sites of electrode during the initial stage of the methanol oxidation reaction.[39] As the oxidation reactions occur, the current density continues to decrease but the trend become slow and the CQDs-Pt@Bi_2WO_6/FTO electrode shows a lower declining rate when compared with the Pt@Bi_2WO_6/FTO electrode. This is more evidence that the introduction of CQDs is beneficial for improving the catalyst tolerance towards CO.

EIS was used to further evaluate the intrinsic behavior of the anodic and photo-anodic processes. The charge transfer resistance of the electrode can be deduced by calculating the diameter of the primary semicircle. The Nyquist plots of EIS for the Pt@Bi_2WO_6/FTO and CQDs-Pt@Bi_2WO_6/FTO electrodes are shown in Fig. 7d. It was observed that the semicircle radius on the Nyquist plots of the EIS obtained for the sensitized CQDs electrode are much smaller than the other electrodes whether they were under light irradiation or not, clearly indicating that the incorporation of CQDs results in the improved conductivity of the electrode. Furthermore, in contrast to the dark state, the resistances of the two types of electrodes were reduced under solar light irradiation, which means that the synergistic effects between the electro-catalytic process and photoelectro-catalytic process are beneficial for the charge transfer in methanol oxidation. Herein, it is reported that the CQDs-Pt@Bi_2WO_6/FTO electrode has less impedance, which is consistent with the *I–t* curve results.

In order to explore the synergistic effect of the photocatalytic and electrocatalytic oxidation methanol, the current densities

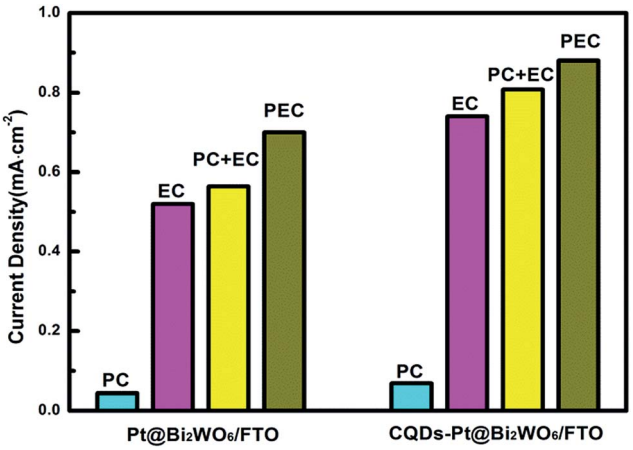

Fig. 8 The current density produced by the different catalytic actions.

produced *via* photocatalysis, electrocatalysis and photoelectron-catalysis on the two types of electrodes were summed up in Fig. 8. The current density produced by photoelectron-catalysis is greater than the sum of the current densities induced by photocatalysis and electrocatalysis, respectively. Undoubtedly, the increment of the current density may be attributed to a synergistic effect between the photocatalytic and electro-catalytic oxidation of methanol.

On the basis of the above experimental results and the literature,[37,40] a schematic representation of photoelectro-catalytic oxidation of methanol at the CQDs-Pt@Bi_2WO_6/FTO electrode under light irradiation is given in Fig. 9. When the electrode is exposed to solar light irradiation, the photogenerated electrons (e^-) and holes (h^+) are obtained in photocatalyst Bi_2WO_6. The holes (h^+) produced in the valence band of Bi_2WO_6 will migrate to the Pt particles, then oxidize the methanol and produce CO_2 and H_2O. The photoelectro-catalytic reaction of methanol oxidation on the Pt particles and Bi_2WO_6 nanoplates is:

$$2Bi_2WO_6 + h\nu \rightarrow Bi_2WO_6\ (e^-) + Bi_2WO_6\ (h^+) \quad (1)$$

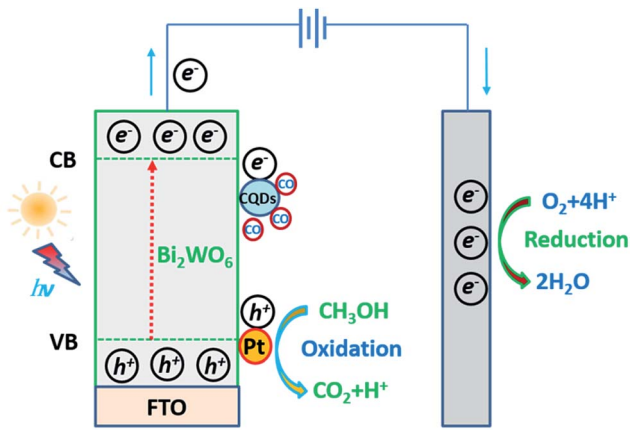

Fig. 9 A schematic representation of the photoelectro-catalytic oxidation of methanol using the CQDs-Pt@Bi_2WO_6/FTO electrode under solar light irradiation.

Open Access Article. Published on 22 May 2017. Downloaded on 12/6/2025 2:02:47 AM.
This article is licensed under a Creative Commons Attribution 3.0 Unported Licence.

$$Pt + xBi_2WO_6\,(h^+) + CH_3OH + H_2O \rightarrow Pt + xBi_2WO_6 + (6 - x)\,e^- + CO_2 + 6H^+ \quad (2)$$

Meanwhile, the Pt particles and the sensitized CQDs receive the photogenerated electrons (e^-) produced in the conduction band of Bi_2WO_6, and the oxygen reduction reaction (ORR) takes place at those cathodic sites. The ORR of O_2 is:

$$Pt + 3/2O_2 + xBi_2WO_6\,(e^-) + (6 - x)\,e^- + 6H^+ \rightarrow Pt + xBi_2WO_6 + 3H_2O \quad (3)$$

$$CQDs + 3/2O_2 + xBi_2WO_6\,(e^-) + (6 - x)\,e^- + 6H^+ \rightarrow CQDs + xBi_2WO_6 + 3H_2O \quad (4)$$

Certainly, some photogenerated electrons (e^-) will transfer to the counter electrode *via* the external circuit and react with O_2 and H^+ to form water.

Apart from capture and transfer of the photo-generated carriers, the sensitized CQDs on the CQDs-Pt@Bi_2WO_6/FTO electrode can broaden the spectral absorption range of Bi_2WO_6. Simultaneously, during the methanol oxidation process, the sensitized CQDs are the preferred adsorption sites for the intermediate carbonaceous species (such as: CO). Therefore, the final CQDs-Pt@Bi_2WO_6/FTO electrode, which combines an enhanced absorption ability, fast charge transfer rate and outstanding synergetic catalytic effect between Pt and holes, can significantly inhibit the fast recombination of electron–hole pairs and improve the photoelectro-catalytic efficiency for methanol oxidation.

4. Conclusions

In the present work, we have synthesized Bi_2WO_6 nanoplates on FTO *via* a hydrothermal method and then fabricated a CQDs-Pt@Bi_2WO_6/FTO electrode by loading Pt particles and doping carbon quantum dots onto Bi_2WO_6 nanoplates, respectively. The Pt particles distributed on the Bi_2WO_6 nanoplates produced a remarkable photoelectro-catalytic response for methanol oxidation due to the broadened light absorption range and improved charge transfer efficiency under light irradiation. When compared with the Pt@Bi_2WO_6/FTO electrode, we found that the sensitized CQDs on Bi_2WO_6/FTO or Pt@Bi_2WO_6/FTO electrode can help to increase their optical absorption properties and improved the mobility of the photocarriers. More importantly, the CQDs act as the preferential adsorption sites for the intermediate carbonaceous species, such as CO, during methanol oxidation that can alleviate CO poisoning towards the electrocatalyst. Our results provide a new pathway to developing novel visible-light-driven photoelectro-catalysts for applications in direct methanol fuel cells.

Acknowledgements

The financial support from Zhejiang scientific and technological projects (No. 2009R50002-20) is gratefully acknowledged.

References

1 Z. H. Zhang, Y. Yuan, Y. J. Fang, L. H. Liang, H. C. Ding, G. Y. Shi and L. T. Jin, *J. Electroanal. Chem.*, 2007, **610**, 179–185.
2 A. Polo, M. C. Santos, R. B. de Souza and W. Alves, *J. Power Sources*, 2011, **196**, 872–876.
3 G. H. Song, M. Q. Shi, Y. Q. Chu and C. A. Ma, *Electrochim. Acta*, 2013, **112**, 53–58.
4 K. Rokesh, A. Pandikumar, S. C. Mohan and K. Jothivenkatachalam, *J. Alloys Compd.*, 2016, **680**, 633–641.
5 Y. F. Hao, X. D. Wang, Y. Y. Zheng, J. F. Shen, J. H. Yuan, A. J. Wang, L. Niu and S. T. Huang, *Electrochim. Acta*, 2016, **198**, 127–134.
6 H. X. Zhong, H. M. Zhang, Z. Xu, Y. F. Tang and J. X. Mao, *ChemSusChem*, 2012, **5**, 1698–1702.
7 E. Akgül, A. Gülce and H. Gülce, *J. Electroanal. Chem.*, 2012, **668**, 73–82.
8 K. Drew, G. Girishkumar, K. Vinodgopal and P. V. Kamat, *J. Phys. Chem. B*, 2005, **109**, 11851–11857.
9 A. Pandikumar, S. Murugesan and R. Ramaraj, *ACS Appl. Mater. Interfaces*, 2010, **2**, 1912–1917.
10 W. T. Chen, Y. K. Lin, T. T. Yang, Y. C. Pu and Y. J. Hsu, *Chem. Commun.*, 2013, **49**, 8486–8488.
11 C. Q. Wang, R. R. Yue, H. W. Wang, C. E. Zou, J. Du, F. X. Jiang, Y. K. Du, P. Yang and C. Y. Wang, *Int. J. Hydrogen Energy*, 2014, **39**, 5764–5771.
12 M. G. Hosseini and M. M. Momeni, *Electrochim. Acta*, 2012, **70**, 1–9.
13 Q. S. Wu, Y. Cui, L. M. Yang, G. Y. Zhang and D. Z. Gao, *Sep. Purif. Technol.*, 2015, **142**, 168–175.
14 J. Su, C. L. Xie, C. Chen, Y. Yu, G. Kennedy, G. A. Somorjai and P. D. Yang, *J. Am. Chem. Soc.*, 2016, **138**, 11568–11574.
15 D. V. Arulmani, J. I. Eastcott, S. G. Mavilla and E. B. Easton, *J. Power Sources*, 2014, **247**, 890–895.
16 H. J. Yu, Y. F. Zhao, C. Zhou, L. Shang, Y. Peng, Y. H. Cao, L. Z. Wu, C. H. Tung and T. R. Zhang, *J. Mater. Chem. A*, 2014, **2**, 3344–3351.
17 W. N. Shi, X. F. Zhang, J. Brillet, D. K. Huang, M. Li, M. K. Wang and Y. Shen, *Carbon*, 2016, **105**, 387–393.
18 Z. F. Zhao, T. Butburee, P. Peerakiathajohn, M. Q. Lyu, S. C. Wang, L. Z. Wang and H. J. Zheng, *ChemistrySelect*, 2016, **1**, 2772–2777.
19 H. Wang, Z. Y. Wei, H. Matsui and S. Q. Zhou, *J. Mater. Chem. A*, 2014, **2**, 15740–15745.
20 J. Di, J. X. Xia, M. X. Ji, B. Wang, X. W. Li, Q. Zhang, Z. G. Chen and H. M. Li, *ACS Sustainable Chem. Eng.*, 2016, **4**, 136–146.
21 J. Di, J. X. Xia, M. X. Ji, L. Xu, S. Yin, Q. Zhang, Z. G. Chen and H. M. Li, *Carbon*, 2016, **98**, 613–623.
22 J. X. Xia, J. Di, H. T. Li, H. Xu, H. M. Li and S. J. Guo, *Appl. Catal., B*, 2016, **181**, 260–269.
23 J. Di, J. X. Xia, Y. P. Ge, H. P. Li, H. Y. Ji, H. Xu, Q. Zhang, H. M. Li and M. N. Li, *Appl. Catal., B*, 2015, **168–169**, 51–61.
24 J. Di, J. X. Xia, M. X. Ji, H. P. Li, H. M. Li and R. Chen, *Nanoscale*, 2015, **7**, 11433–11443.

 This journal is © The Royal Society of Chemistry 2017

Open Access Article. Published on 22 May 2017. Downloaded on 12/6/2025 2:02:47 AM.
This article is licensed under a Creative Commons Attribution 3.0 Unported Licence.

25 D. Tang, H. C. Zhang, H. Huang, R. H. Liu, Y. Z. Han, Y. Liu, C. Y. Tong and Z. H. Kang, *Dalton Trans.*, 2013, **42**, 6285–6289.
26 Z. Y. Shih, A. P. Periasamy, P. C. Hsu and H. T. Chang, *Appl. Catal., B*, 2013, **132–133**, 363–369.
27 Z. F. Zhao, T. Butburee, M. Q. Lyv, P. Peerakiathajohn, S. C. Wang, L. Z. Wang and H. J. Zheng, *RSC Adv.*, 2016, **6**, 68204–68210.
28 B. C. M. Martindale, G. A. M. Hutton, C. A. Caputo and E. Reisner, *J. Am. Chem. Soc.*, 2015, **137**, 6018–6025.
29 C. Ng, A. Iwase, Y. H. Ng and R. Amal, *J. Phys. Chem. Lett.*, 2012, **3**, 913–918.
30 H. T. Li, R. H. Liu, Y. Liu, H. Huang, H. Yu, H. Ming, S. Y. Lian, S. T. Lee and Z. H. Kang, *J. Mater. Chem.*, 2012, **22**, 17470–17475.
31 Y. Zhou, X. J. Zhang, Q. Zhang, F. Dong, F. Wang and Z. Xiong, *J. Mater. Chem. A*, 2014, **2**, 16623–16631.
32 P. R. Kasturi, R. K. Selvan and Y. S. Lee, *RSC Adv.*, 2016, **6**, 62680–62694.
33 L. T. Ye, Z. S. Li, X. F. Zhang, F. L. Lei and S. Lin, *J. Mater. Chem. A*, 2014, **2**, 21010–21019.
34 C. Y. Zhai, M. S. Zhu, F. Z. Pang, D. Bin, C. Lu, M. C. Goh, P. Yang and Y. K. Du, *ACS Appl. Mater. Interfaces*, 2016, **8**, 5972–5980.
35 R. F. Tang, H. F. Su, S. X. Duan, Y. W. Sun, L. Li, X. X. Zhang, S. Y. Zeng and D. Z. Sun, *RSC Adv.*, 2015, **5**, 41949–41960.
36 N. M. Vuong, J. L. Reynolds, E. Conte and Y. Lee, *J. Phys. Chem. C*, 2015, **119**, 24323–24331.
37 T. Wang, J. Tang, S. C. Wu, X. L. Fan and J. P. He, *J. Power Sources*, 2014, **248**, 510–516.
38 L. T. Ye, Z. S. Li, L. Zhang, F. L. Lei and S. Lin, *J. Colloid Interface Sci.*, 2014, **433**, 156–162.
39 M. D. Dios, V. Salgueirino, M. Perez-Lorenzo and M. A. Correa-Duarte, *J. Chem. Educ.*, 2012, **89**, 280–283.
40 W. Li, Y. Bai, F. J. Li, C. Liu, K. Chan, X. Feng and X. H. Lu, *J. Mater. Chem.*, 2012, **22**, 4025–4031.